



Nanostructured $\text{Li}_3\text{V}_2(\text{PO}_4)_3$ cathode supported on reduced graphene oxide for lithium-ion batteries

Bo Pei ^{a,b}, Zhongqing Jiang ^b, Weixin Zhang ^{a,*,**}, Zeheng Yang ^a, Arumugam Manthiram ^{b,*}

^a School of Chemical Engineering, Hefei University of Technology, Hefei, Anhui 230009, PR China

^b Electrochemical Energy Laboratory and Materials Science and Engineering Program, Texas Materials Institute, The University of Texas at Austin, Austin, TX 78712, USA



HIGHLIGHTS

- $\text{Li}_3\text{V}_2(\text{PO}_4)_3$ nanoparticles supported on reduced graphene have been synthesized.
- Insertion of CTAB enhances the dispersibility of graphene oxide.
- $\text{Li}_3\text{V}_2(\text{PO}_4)_3/\text{reduced graphene nanocomposite}$ offers high rate capability.
- Tight contact between $\text{Li}_3\text{V}_2(\text{PO}_4)_3$ and reduced graphene oxide enhances performance.

ARTICLE INFO

Article history:

Received 11 February 2013

Received in revised form

27 March 2013

Accepted 28 March 2013

Available online 6 April 2013

Keywords:

Lithium-ion batteries

Lithium vanadium phosphate

Solvothermal synthesis

Graphene oxide

Electrochemical performance

ABSTRACT

$\text{Li}_3\text{V}_2(\text{PO}_4)_3/\text{reduced graphene oxide}$ (designated as $\text{Li}_3\text{V}_2(\text{PO}_4)_3/\text{rGO}$) and $\text{Li}_3\text{V}_2(\text{PO}_4)_3/\text{reduced modified graphene oxide}$ (designated as $\text{Li}_3\text{V}_2(\text{PO}_4)_3/\text{rmGO}$) nanocomposites have been synthesized by a solvothermal method, followed by post-heat treatment at 800 °C, and explored as cathodes in lithium-ion cells. Lamellar GO sheets were modified with cetyltrimethylammonium bromide (CTAB) to form mGO with good dispersibility. The $\text{Li}_3\text{V}_2(\text{PO}_4)_3/\text{rGO}$ (~ 350 nm particles) and $\text{Li}_3\text{V}_2(\text{PO}_4)_3/\text{rmGO}$ (~ 200 nm particles) nanocomposite cathodes display discharge capacities of, respectively, 170 and 186 mA h g⁻¹ at 0.1 C rate and 118 and 135 mA h g⁻¹ at 10 C rate between 3.0 and 4.8 V. The higher discharge capacity and rate capability of $\text{Li}_3\text{V}_2(\text{PO}_4)_3/\text{rmGO}$ compared to $\text{Li}_3\text{V}_2(\text{PO}_4)_3/\text{rGO}$ are ascribed mainly to the smaller particle size of $\text{Li}_3\text{V}_2(\text{PO}_4)_3$ and the tight contact between the $\text{Li}_3\text{V}_2(\text{PO}_4)_3$ nanoparticles and the rmGO sheets. The tight contact enables fast electron transport through the underlying rmGO sheets to $\text{Li}_3\text{V}_2(\text{PO}_4)_3$ nanoparticles.

© 2013 Elsevier B.V. All rights reserved.

1. Introduction

There is an increasing demand for rechargeable batteries with higher energy and better safety at an affordable cost for electric vehicles (EVs) and grid storage of electricity produced by renewable energies [1,2]. Lithium metal phosphates such as LiFePO_4 [3], LiMnPO_4 [4], and $\text{Li}_3\text{V}_2(\text{PO}_4)_3$ [5] are appealing in this regard as they offer much better thermal stability compared to the oxide cathodes [6,7]. Among the phosphates, the NASICON-type monoclinic $\text{Li}_3\text{V}_2(\text{PO}_4)_3$ has offered several advantages such as higher theoretical capacity of 197 mA h g⁻¹ and higher operating voltages of up to 4.0 V compared with LiFePO_4 [5,8]. Furthermore, the NASICON structure has interconnected interstitial space, which is favorable to

stabilize the structure and facilitate fast lithium-ion conduction [9]. However, like LiFePO_4 [10], $\text{Li}_3\text{V}_2(\text{PO}_4)_3$ has a low electronic conductivity (2.4×10^{-7} S cm⁻¹ at room temperature) [11], which largely limits its rate performance. Some approaches such as reducing the particle size [12], doping with other metal ions [13,14], and coating with conductive agents [15,16] have been pursued in the literature to overcome this problem.

Graphene is a well-defined two-dimensional substrate for growing and anchoring electrode materials for energy storage applications owing to its superior electronic conductivity [17,18], remarkable structural flexibility [19,20], and high mechanical strength [21]. Some electrode materials such as Fe_3O_4 , Co_3O_4 , and $\text{LiMn}_{1-x}\text{Fe}_x\text{PO}_4$ have been decorated with graphene sheets and exhibited enhanced electrochemical properties [22–24]. Recently, Cao et al. [22] utilized a one-step strategy to prepare graphene/ Fe_3O_4 nanocomposites under hydrothermal conditions, where the reduction process of graphite oxide sheets into graphene was

* Corresponding author. Tel.: +1 512 471 1791; fax: +1 512 471 7681.

** Corresponding author. Tel./fax: +86 551 2901450.

E-mail address: rmanth@mail.utexas.edu (A. Manthiram).

accompanied by the generation of Fe_3O_4 nanoparticles, and the graphene/ Fe_3O_4 nanocomposites exhibited improved cycling stability and rate performances. Cui et al. [24] reported that $\text{LiMn}_{1-x}\text{Fe}_x\text{PO}_4$ nanorods on reduced graphene oxide sheets synthesized by a solvothermal method in N,N-dimethylformamide (DMF) solvent display a discharge capacity of 155 mA h g^{-1} at 0.5 C rate. Yang et al. [25] adopted a sol-gel method followed by a high-temperature reaction to synthesize $\text{Li}_3\text{V}_2(\text{PO}_4)_3$ /graphene nanocomposites using partially reduced graphene oxide as the conductive agent, which showed a discharge capacity of ~170 mA h g^{-1} at 0.1 C rate.

In this paper, we report the use of surfactant cetyltrimethylammonium bromide (CTAB) to modify graphene oxide (GO). The positively charged ammonium ions of CTAB can come close to the negatively charged carboxyl group on GO sheets through Coulombic attraction while the negatively-charged bromide of CTAB repels the other neighboring GO sheets, resulting in CTAB-insertion into the lamellar GO sheets and facilitating the dispersibility of the modified graphene oxide (mGO). Accordingly, we have prepared $\text{Li}_3\text{V}_2(\text{PO}_4)_3/\text{rmGO}$ nanocomposites with mGO as a supporting substrate via a solvothermal method followed by post heat treatment, rather than using GO as carrier for the guest materials. When used as cathode materials in lithium-ion batteries, the $\text{Li}_3\text{V}_2(\text{PO}_4)_3/\text{rmGO}$ nanocomposites show enhanced electrochemical performance compared to $\text{Li}_3\text{V}_2(\text{PO}_4)_3/\text{rGO}$, demonstrating that the use of mGO instead of GO is beneficial for improving the electrochemical properties of $\text{Li}_3\text{V}_2(\text{PO}_4)_3$ /graphene nanomaterials.

2. Experimental

2.1. Preparation of graphene oxide (GO)

Graphene oxide was synthesized from natural graphite by a modified Hummers method [26]. Graphite (5 g, 300 mesh) and NaNO_3 (2.5 g, Fisher) were mixed in 115 mL of concentrated H_2SO_4 (95%, Fisher) in a 500 mL flask. The mixture was stirred for 30 min in an ice bath. Potassium permanganate (15 g, Fisher) was then added gradually under stirring so that the temperature of the mixture remained below 20 °C. The mixture was stirred at room temperature overnight, and 180 mL of de-ionized water was slowly

added to the mixture, followed by vigorous stirring at 98 °C for one day. Afterward, 80 mL of H_2O_2 (30%, Fisher) was added to the mixture. The mixture was then washed by rinsing and centrifugation with 5% HCl solution and then deionized (DI) water for several times, filtered, and dried under vacuum to obtain the graphene oxide (GO) powder.

2.2. Preparation of modified graphene oxide (mGO)

150 mg of GO was dispersed into 10 mL of H_2O , which gave a brown homogeneous suspension after 4 h of ultrasonication. Typically, 10 mL of the resulting GO suspension (15 mg mL^{-1}) and 20 mL of cetyltrimethylammonium bromide solution (CTAB solution, 0.2 M, Fisher) were added into a 50 mL flask, and the mixture was stirred at room temperature for 3 days, then filtered, washed, and dried under vacuum at 60 °C to obtain the modified graphene oxide (mGO).

2.3. Synthesis of $\text{Li}_3\text{V}_2(\text{PO}_4)_3/\text{rGO}$ and $\text{Li}_3\text{V}_2(\text{PO}_4)_3/\text{rmGO}$

The $\text{Li}_3\text{V}_2(\text{PO}_4)_3/\text{rmGO}$ nanocomposites were prepared by a solvothermal process. The reactants were LiH_2PO_4 (Fisher) and $\text{V}(\text{C}_5\text{H}_7\text{O}_2)_3$ (Fisher) in a stoichiometric ratio of 3:2. First, 0.94 g of LiH_2PO_4 was dissolved in 10 mL of deionized water with stirring. Then, the mGO (0.030 g) was suspended in the above solution by ultrasonication for 1 h to form a brown suspension. 2.09 g of $\text{V}(\text{C}_5\text{H}_7\text{O}_2)_3$ was dissolved in 25 mL of ethanol under stirring at 70 °C until a brown solution was formed. Thereafter, 5 mL of ethylene glycol (EG, Alfa Aesar) and the mGO suspension were added to the brown solution of $\text{V}(\text{C}_5\text{H}_7\text{O}_2)_3$ with vigorous stirring for 10 min. The mixture was then transferred to a 50 mL Teflon-lined stainless steel autoclave and heated at 180 °C for 24 h. EG was used as reductant to avoid the oxidation of V^{III} and also to partially reduce mGO. After the solvothermal reaction, the autoclave was cooled to room temperature naturally. The blue gel suspension was heated on a hot plate at 80 °C under stirring to render a $\text{Li}_3\text{V}_2(\text{PO}_4)_3/\text{partial rmGO}$ precursor.

The prepared $\text{Li}_3\text{V}_2(\text{PO}_4)_3/\text{partial rmGO}$ precursor was decorated with carbon coating through post-heat treatment. Sucrose (Fisher) in a 5:100 weight ratio to the precursor was initially dissolved in deionized water to form a transparent solution, and then

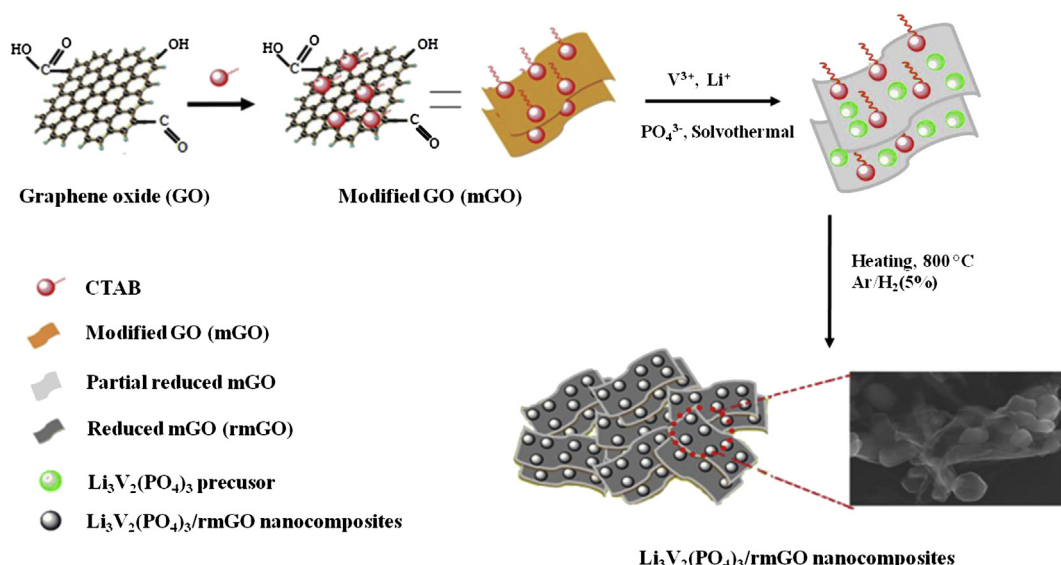


Fig. 1. Schematic diagram of the synthesis process of the $\text{Li}_3\text{V}_2(\text{PO}_4)_3/\text{rmGO}$ nanocomposites.

mixed with the precursor at room temperature by 20 min of ultrasonication to form a uniform slurry. The slurry samples were dried at 80 °C for 12 h to remove the excess water. The dry samples were first heated at 350 °C for 4 h (heating rate: 3.0 °C min⁻¹) and then at 800 °C for 10 h (4.0 °C min⁻¹) under a 5:95 hydrogen–argon atmosphere in a tube furnace. The formation process of the Li₃V₂(PO₄)₃/rmGO is presented in Fig. 1.

For the synthesis of Li₃V₂(PO₄)₃/reduced graphene oxide (rGO), the procedure was identical except that GO instead of mGO was used in the solvothermal reaction.

2.4. Characterization of the samples

X-ray diffraction (XRD) was performed on a Philips X-ray diffractometer with filtered Cu K α radiation. Scanning electron microscopy (SEM) images were obtained on a Hitachi S-5500 Scanning electron microscope. Transmission electron microscopy (TEM) and high-resolution transmission electron microscopy (HRTEM) were carried out on a JEOL 2010F transmission electron microscope. Fourier Transform Infrared (FTIR) spectra were collected on a PerkinElmer BX FTIR spectrometer. Pellets for FTIR analysis were prepared by grinding and pressing the samples with dried KBr powder. The carbon contents in the samples were obtained on a Perkin–Elmer Series II CHNS/O (USA) elemental analyzer.

2.5. Electrochemical measurements

Electrochemical performances were evaluated with CR2032 coin cells at 4.3–3.0 V or 4.8–3.0 V with an Arbin battery cycler. The coin cells were fabricated with the Li₃V₂(PO₄)₃/rmGO or Li₃V₂(PO₄)₃/rGO cathode, metallic lithium anode, 1 M LiPF₆ in 1:1 diethyl carbonate/ethylene carbonate electrolyte, and Celgard polypropylene separator. The cathodes were prepared by mixing 80 wt.% of pristine Li₃V₂(PO₄)₃/rmGO or Li₃V₂(PO₄)₃/rGO nanocomposites with 10 wt.% of conductive Super P carbon (SP) and 10 wt.% of polyvinylidene fluoride (PVDF) binder, rolling the mixture into thin sheets, and cutting them into circular electrodes of 0.64 cm² area. The electrodes typically had an active material mass of 5–6 mg, and were dried under vacuum at 120 °C for more than 3 h before assembling the cells in an argon-filled glove box. Cyclic voltammetry data were obtained on a Radiometer Analytical Voltalab PGZ402 Potentiostat with a step of 0.05 mV s⁻¹. Electrochemical impedance spectroscopy (EIS) measurements were

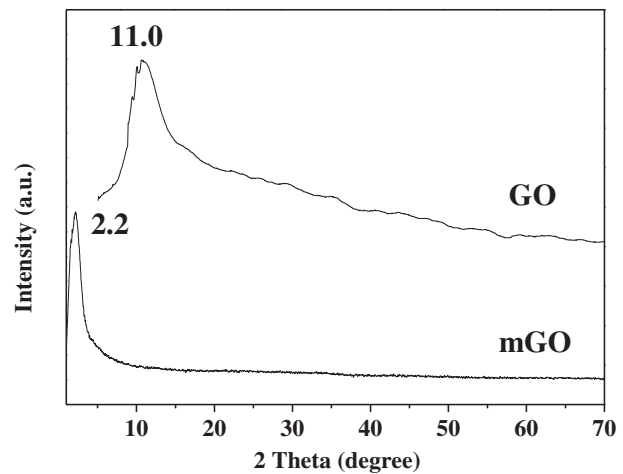


Fig. 3. XRD patterns of GO and mGO.

collected with a computer interfaced HP 4192A LF Impedance Analyzer in the frequency range of 100 kHz to 10 mHz with an excitation voltage of 10 mV.

3. Results and discussion

Fig. 1 shows the schematic of a two-step reaction for the synthesis of Li₃V₂(PO₄)₃ nanoparticles wrapped by rmGO. The first step is to modify GO, which was prepared by a modified Hummers method [26] in the presence of CTAB. It is believed that the positively charged ammonium ions of CTAB can attract the negatively charged carboxyl group of GO via Coulombic forces, resulting in an isolation of the lamellar GO sheets due to the CTAB insertion. Similar observations have also been reported by Müllen et al. [27] on the insertion into lamellar GO sheets by tetradodecylammonium bromide (TAB). The second step is to synthesize Li₃V₂(PO₄)₃ nanoparticles decorated by the mGO sheets via a solvothermal reaction of LiH₂PO₄ and V(C₅H₇O₂)₃ at 180 °C. Ethylene glycol (EG) was added as solvent to avoid oxidation of V^{III} and also to partially reduce mGO through the removal of some epoxide and hydroxyl functional groups [28]. The mGO consists of sufficient oxygen-containing groups [29], such as carboxyl, hydroxyl, and epoxide groups, which provide sites for the adsorption of cations (V³⁺ and Li⁺) and nanoparticles nucleation to achieve uniform Li₃V₂(PO₄)₃

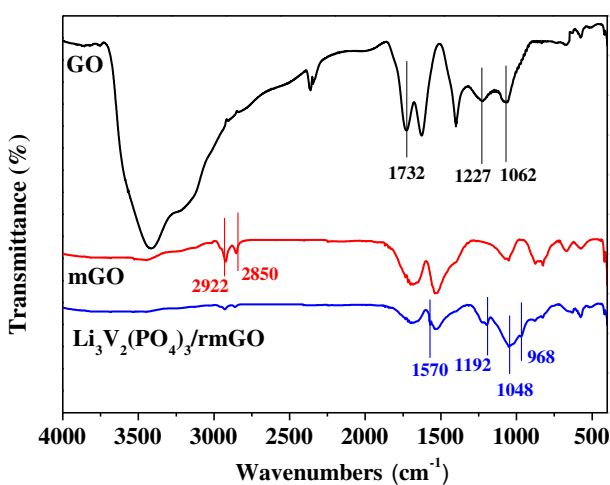


Fig. 2. FT-IR spectra of GO, mGO, and Li₃V₂(PO₄)₃/rmGO.

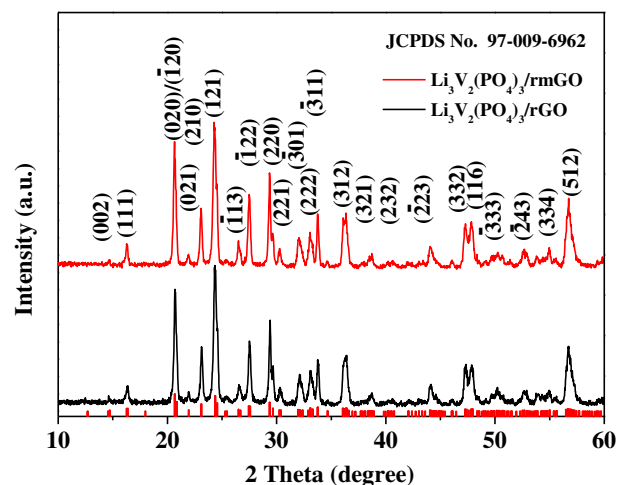


Fig. 4. XRD patterns of Li₃V₂(PO₄)₃/rGO and Li₃V₂(PO₄)₃/rmGO.

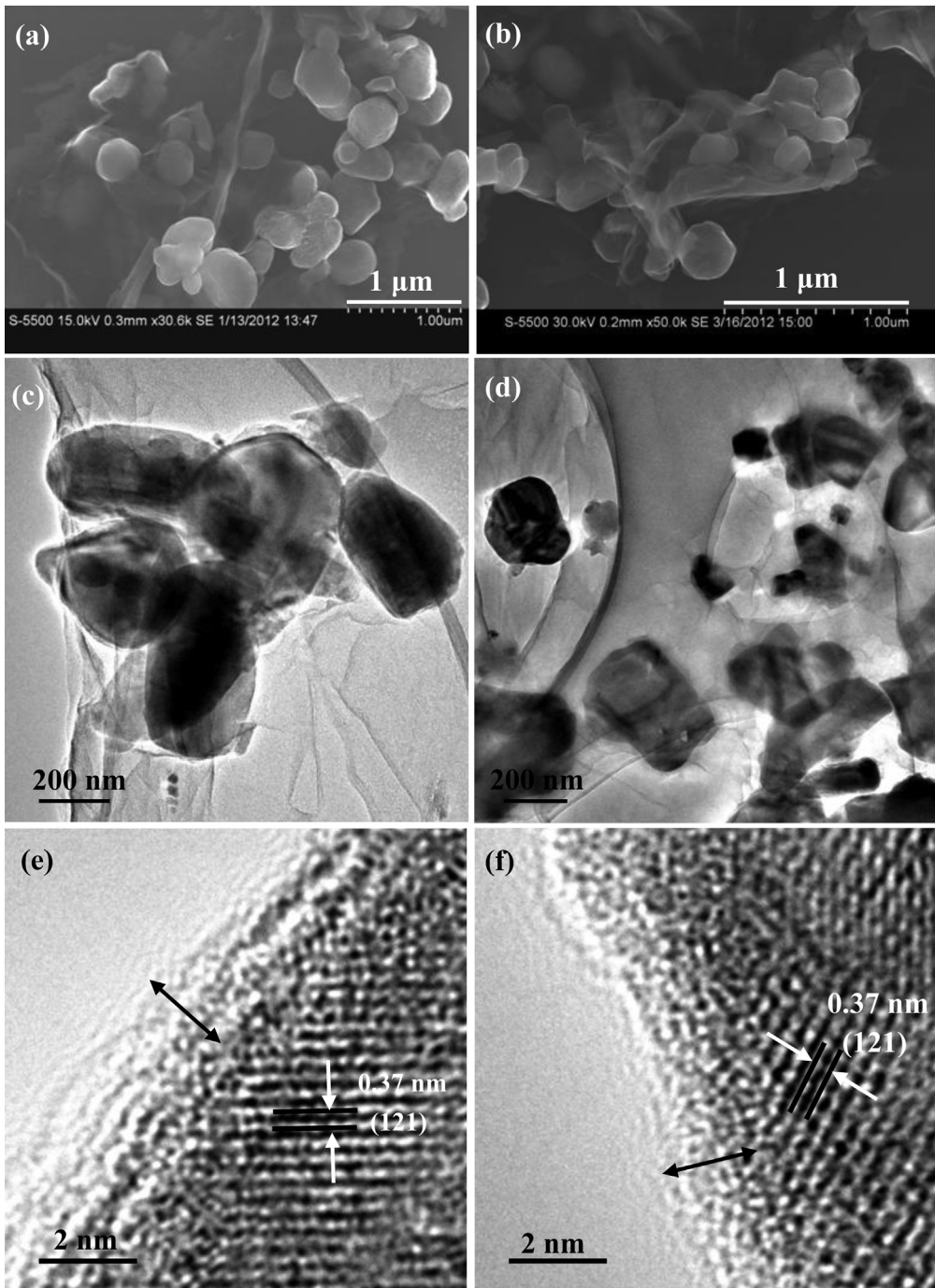


Fig. 5. SEM images of $\text{Li}_3\text{V}_2(\text{PO}_4)_3/\text{rGO}$ (a) and $\text{Li}_3\text{V}_2(\text{PO}_4)_3/\text{rmGO}$ (b), and TEM images of $\text{Li}_3\text{V}_2(\text{PO}_4)_3/\text{rGO}$ (c) and $\text{Li}_3\text{V}_2(\text{PO}_4)_3/\text{rmGO}$ (d). Also shown are the corresponding HR-TEM images (e and f) of c and d.

precursors on the mGO surface. The resulting nanoparticles could be bonded to the partial rmGO by V—O—C bonds at the remaining oxygen sites and by van der Waals interactions with the aromatic regions of the partial rmGO. The transformation of $\text{Li}_3\text{V}_2(\text{PO}_4)_3/\text{partial rmGO}$ precursor to $\text{Li}_3\text{V}_2(\text{PO}_4)_3/\text{rmGO}$ nanocomposites is through a post-heat treatment.

Fourier transform infrared (FT-IR) spectra of GO and mGO are shown in Fig. 2. The observed representative peaks of GO include the bands at 1062 cm^{-1} (C—O stretching vibration of epoxide), 1227 cm^{-1} (C—OH stretching for phenolic), and 1732 cm^{-1} (C—O stretching of carbonyl and carboxyl groups located at the edges of the GO networks). These characteristic peaks of GO confirm the

presence of the oxygen-containing functional groups in carbon frameworks [30]. For mGO, the bands at 2922 and 2850 cm^{-1} are assigned to $-\text{CH}_2$ and $-\text{CH}_3$, both are the characteristic peaks of CTAB, confirming the existence of CTAB in mGO [31]. It may be noted that the intensities of the representative peaks at 1062 and 1732 cm^{-1} of GO are lower in mGO than in GO due to the presence of some CTAB and the relatively lower concentration of GO in mGO. Also, a very small peak present at 1227 cm^{-1} in GO is hardly observed in mGO due to the lower concentration of GO in mGO.

XRD patterns of GO and mGO are shown in Fig. 3. GO and mGO exhibit reflections at 11.0° and 2.2° , which are assigned to the (001) planes. Bragg's law ($2d_{hkl} \sin \theta_{hkl} = \lambda$) can be used to calculate the

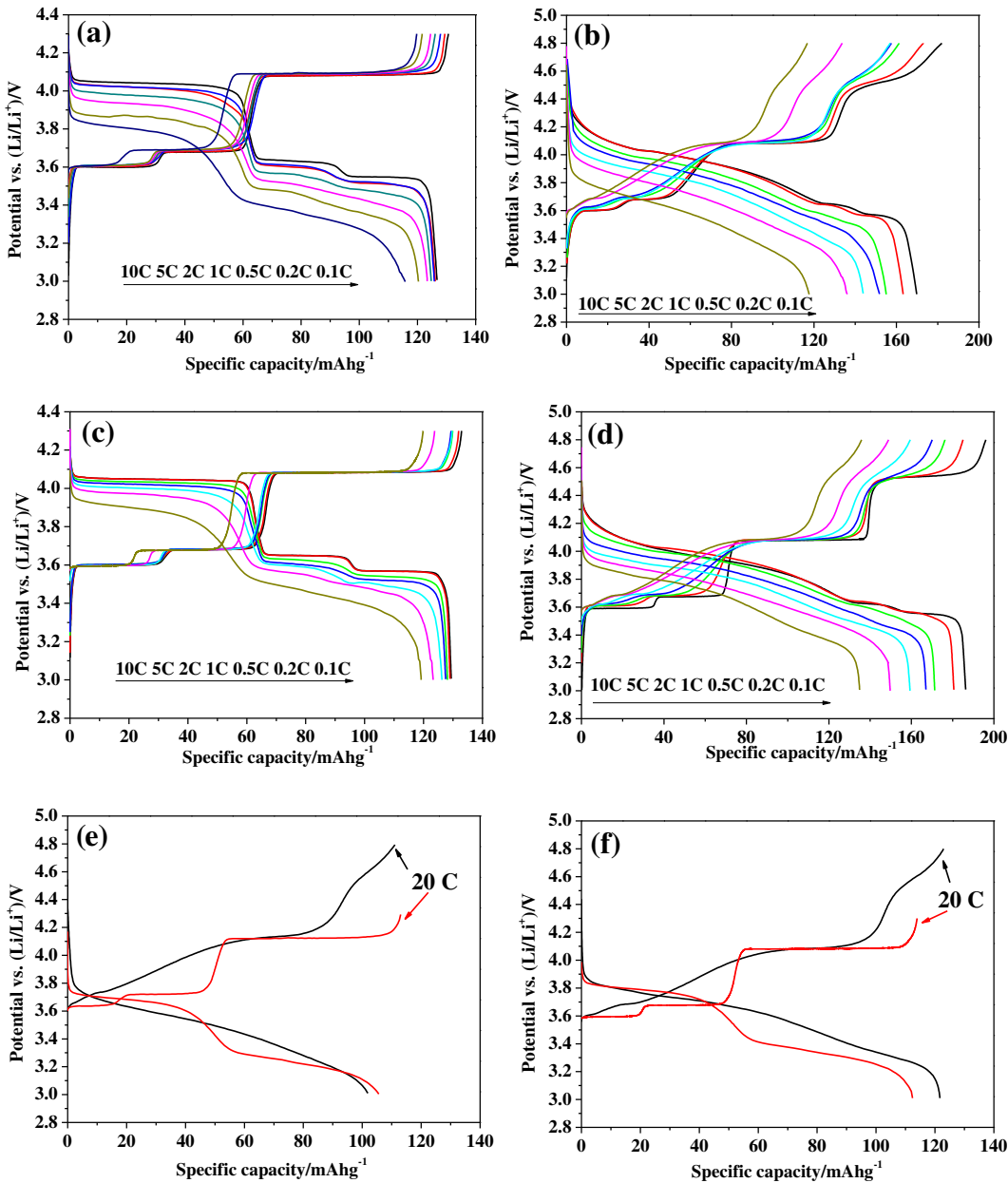


Fig. 6. Initial charge–discharge curves of the nanocomposites in the potential ranges of 3.0–4.3 V and 3.0–4.8 V: (a) and (b) $\text{Li}_3\text{V}_2(\text{PO}_4)_3/\text{rGO}$; (c) and (d) $\text{Li}_3\text{V}_2(\text{PO}_4)_3/\text{rmGO}$. Initial charge–discharge curves of $\text{Li}_3\text{V}_2(\text{PO}_4)_3/\text{rGO}$ (e) and $\text{Li}_3\text{V}_2(\text{PO}_4)_3/\text{rmGO}$ (f) at 20 C rate ($\text{Li}_3\text{V}_2(\text{PO}_4)_3:\text{SP}:\text{PVDF}$ in a ratio of 60:30:10).

distance d_{hkl} between atomic planes in a crystal, where λ is the wavelength of the incident X-ray beam (0.15406 nm) and $2\theta_{hkl}$ is the diffraction angle. The average interlayer distances d_{hkl} of GO and mGO are calculated to be, respectively, 0.8 and 4.0 nm. The significant increase of the interlayer distance in mGO confirms that the GO sheets were expanded because of the insertion of the surfactant CTAB into the lamellar GO sheets via strong electrostatic interactions.

The XRD patterns of $\text{Li}_3\text{V}_2(\text{PO}_4)_3/\text{rGO}$ and $\text{Li}_3\text{V}_2(\text{PO}_4)_3/\text{rmGO}$ are shown in Fig. 4. The diffraction peaks of both XRD patterns could be indexed well to the monoclinic $\text{Li}_3\text{V}_2(\text{PO}_4)_3$ with the space group of $P2_1/n$ (JCPDS card no. 97-009-6962). The lattice parameters and unit-cell volume of $\text{Li}_3\text{V}_2(\text{PO}_4)_3/\text{rmGO}$ are calculated to be $a = 0.86685$ nm, $b = 0.85961$ nm, $c = 1.20459$ nm, $\beta = 90.13^\circ$, and $V = 0.89760$ nm³, which are very close to those in previous reports [32]. The FT-IR spectra of $\text{Li}_3\text{V}_2(\text{PO}_4)_3/\text{rmGO}$ are shown in Fig. 2. The

band at 968 cm^{-1} is ascribed to the vibration of bonds between V^{3+} and O^{2-} in the VO_6 octahedra. The band at 1048 cm^{-1} corresponds to the P–O bonds of PO_4 tetrahedra. The bands between 1150 and 1250 cm^{-1} can be assigned to the stretching vibrations of terminal PO_4 units. The band at 1570 cm^{-1} corresponds to the aromatic skeletal $\text{C}=\text{C}$ stretching vibration of the graphene sheets [33].

Fig. 5 depicts the SEM and TEM images of $\text{Li}_3\text{V}_2(\text{PO}_4)_3/\text{rGO}$ and $\text{Li}_3\text{V}_2(\text{PO}_4)_3/\text{rmGO}$ nanocomposites. It can be seen from Fig. 5a and b that $\text{Li}_3\text{V}_2(\text{PO}_4)_3$ nanoparticles are anchored on the surface of graphene sheets, and $\text{Li}_3\text{V}_2(\text{PO}_4)_3$ nanoparticles in the $\text{Li}_3\text{V}_2(\text{PO}_4)_3/\text{rmGO}$ nanocomposite have larger contact surface with more flexible rmGO sheets compared with those in the $\text{Li}_3\text{V}_2(\text{PO}_4)_3/\text{rGO}$ nanocomposite. A large quantity of $\text{Li}_3\text{V}_2(\text{PO}_4)_3$ nanoparticles have deposited on both sides of rmGO sheets as shown in Fig. 5b. The average size of the $\text{Li}_3\text{V}_2(\text{PO}_4)_3$ nanoparticles decorated by the graphene sheets in the $\text{Li}_3\text{V}_2(\text{PO}_4)_3/\text{rGO}$ and $\text{Li}_3\text{V}_2(\text{PO}_4)_3/\text{rmGO}$

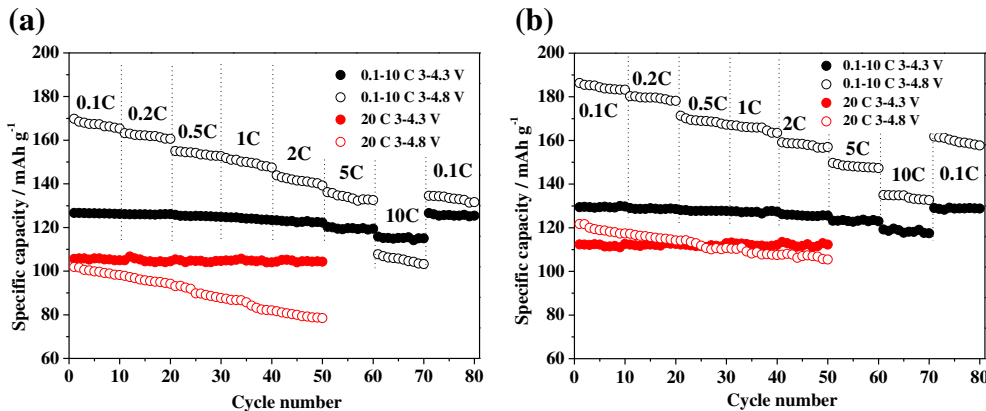


Fig. 7. Rate and cycling performances of Li₃V₂(PO₄)₃/rGO (a) and Li₃V₂(PO₄)₃/rmGO (b). The cells were charged at a rate of 0.2 C to ensure identical conditions for each discharge.

nanocomposites are, respectively, ~350 and ~200 nm, as confirmed by the TEM images shown in Fig. 5c and d. Because the positively charged ammonium and the negatively charged bromide ions of CTAB are, respectively, attractive and repulsive to the negatively charged carboxyl group of GO sheets, the insertion of CTAB into lamellar GO sheets and the expansion of the modified graphene oxide (mGO) occur. Compared with GO, the mGO with good dispersibility provides more sites for the adsorption of cations (V³⁺ and Li⁺) as well as the nucleation and growth of Li₃V₂(PO₄)₃ nanoparticles. Meanwhile, the mGO with good dispersibility has larger contact surface with the Li₃V₂(PO₄)₃ precursor, suppressing the growth of Li₃V₂(PO₄)₃ nanoparticles. Therefore, compared with the Li₃V₂(PO₄)₃/rGO nanocomposites, the Li₃V₂(PO₄)₃/rmGO nanocomposite exhibits a smaller particle size.

The observed width (0.37 nm) of the neighboring lattice fringes in the high-resolution TEM (HRTEM) images (Fig. 5e and f) corresponds to the (121) plane of Li₃V₂(PO₄)₃, demonstrating the well-textured and crystalline nature of Li₃V₂(PO₄)₃ nanoparticles in the Li₃V₂(PO₄)₃/rGO and Li₃V₂(PO₄)₃/rmGO nanocomposites. Fig. 5e and f shows uniform carbon (amorphous region) with a thickness of ~2 nm on the surface of Li₃V₂(PO₄)₃ nanoparticles in the crystalline fringe region, which mainly arises from the decomposition of sucrose. The elemental analysis indicates that the carbon content in the Li₃V₂(PO₄)₃/rGO and Li₃V₂(PO₄)₃/rmGO is 7.82 and 7.96%, respectively, which results from rGO or rmGO and the decomposition of the ethylene glycol and sucrose.

Fig. 6a and b shows the charge–discharge curves of Li₃V₂(PO₄)₃/rGO at various rates from 0.1 to 10 C in the potential ranges of 3.0–4.3 V and 3.0–4.8 V vs. Li/Li⁺, respectively. When the sample is charged to 4.8 V at 0.1 C rate as shown in Fig. 6b, all three Li-ions are

extracted from Li₃V₂(PO₄)₃ over four two-phase electrochemical plateaus at 3.60, 3.68, 4.08, and 4.52 V, which correspond to different phases of Li_xV₂(PO₄)₃, respectively, at $x = 3.0, 2.5, 2.0, 1.0$, and 0 [12]. The first Li-ion is extracted in two steps (at 3.60 and 3.68 V) because of the existence of the ordered phases Li_{2.5}V₂(PO₄)₃ and Li₂V₂(PO₄)₃ with a mixed-valent V³⁺/V⁴⁺ [34]. Then, a single-step removal of the second Li-ion at 4.08 V is observed to form LiV₂(PO₄)₃, which corresponds to the complete oxidation of V³⁺ to V⁴⁺. The third Li-ion is extracted at 4.52 V to form V₂(PO₄)₃, in which vanadium is in a mixed-valent state of V⁴⁺ and V⁵⁺. On the other hand, during discharge, the curves exhibit three plateaus at 3.54, 3.62 and 4.01 V, corresponding to the reversible insertion of all three extracted Li-ions.

Fig. 6c and d shows the initial charge–discharge curves of Li₃V₂(PO₄)₃/rmGO at various rates from 0.1 C to 10 C in the potential ranges of, respectively, 3.0–4.3 V and 3.0–4.8 V vs. Li/Li⁺. With the increase in discharge current density, potential plateaus become shorter and the separation between the charge and discharge plateaus become larger gradually. From Fig. 6a–d, it is clear that the Li₃V₂(PO₄)₃/rmGO nanocomposite presents higher discharge capacities than Li₃V₂(PO₄)₃/rGO. For instance, between 3.0 and 4.3 V, Li₃V₂(PO₄)₃/rmGO displays initial discharge capacities of 129, 128, 123, and 119 mA h g⁻¹, respectively, at 0.1 C, 1 C, 5 C, and 10 C rates, while Li₃V₂(PO₄)₃/rGO exhibits capacities of 127, 125, 120, and 116 mA h g⁻¹ at the corresponding C rates. Between 3.0 and 4.8 V, the initial discharge capacities of the Li₃V₂(PO₄)₃/rmGO nanocomposite at 0.1 C, 1 C, 5 C, and 10 C rates are, respectively, 186, 167, 150, and 135 mA h g⁻¹, whereas the Li₃V₂(PO₄)₃/rGO nanocomposite exhibits, respectively, 170, 152, 136, and 118 mA h g⁻¹. Initial charge–discharge curves of the Li₃V₂(PO₄)₃/rGO and

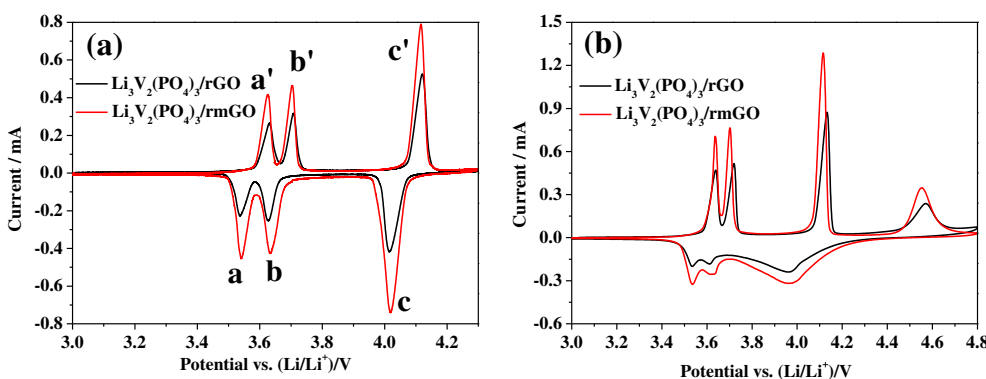


Fig. 8. Cyclic voltammograms of Li₃V₂(PO₄)₃/rGO and Li₃V₂(PO₄)₃/rmGO in the first cycle at a scan rate of 0.05 mV s⁻¹ at 3.0–4.3 V (a) and 3.0–4.8 V (b) (versus Li⁺/Li).

$\text{Li}_3\text{V}_2(\text{PO}_4)_3/\text{rmGO}$ at 20 C rate are shown in Fig. 6e and f when the SP content is increased to 30 wt%. The discharge capacities at 20 C rate are 106 and 112 mA h g⁻¹ between 3.0 and 4.3 V, and 102 and 121 mA h g⁻¹ between 3.0 and 4.8 V for $\text{Li}_3\text{V}_2(\text{PO}_4)_3/\text{rGO}$ and $\text{Li}_3\text{V}_2(\text{PO}_4)_3/\text{rmGO}$, respectively.

Fig. 7 presents the rate capability and cycle performance of $\text{Li}_3\text{V}_2(\text{PO}_4)_3/\text{rGO}$ and $\text{Li}_3\text{V}_2(\text{PO}_4)_3/\text{rmGO}$ in the potential ranges of 3.0–4.3 V and 3.0–4.8 V at different C-rates. The discharge capacities of the two samples decrease as expected with increased discharge rate. Compared with those of the $\text{Li}_3\text{V}_2(\text{PO}_4)_3/\text{rGO}$ nanocomposite, the discharge capacities of the $\text{Li}_3\text{V}_2(\text{PO}_4)_3/\text{rmGO}$ nanocomposite are greatly enhanced at rates from 0.1 C to 10 C, especially at higher current rates, in the potential range of 3.0–4.8 V. When the current density is decreased from 10 C to 0.1 C rate at the end of cycling, the discharge capacities of $\text{Li}_3\text{V}_2(\text{PO}_4)_3/\text{rGO}$ and $\text{Li}_3\text{V}_2(\text{PO}_4)_3/\text{rmGO}$ can still reach, respectively, 135 and 162 mA h g⁻¹ between 3.0 and 4.8 V. With an increase in the SP content to 30 wt%, the capacity retentions after 50 cycles for $\text{Li}_3\text{V}_2(\text{PO}_4)_3/\text{rmGO}$ are 99.9% and 86.7%, respectively, in the potential ranges of 3.0–4.3 V and 3.0–4.8 V at 20 C rate, whereas those of $\text{Li}_3\text{V}_2(\text{PO}_4)_3/\text{rGO}$ are 98.8% and 77.0% in the corresponding potential ranges. The $\text{Li}_3\text{V}_2(\text{PO}_4)_3/\text{rmGO}$ nanocomposite exhibits better rate capability and cycling performance, which is mainly ascribed to the superior dispersibility of mGO, subsequent large contact between the $\text{Li}_3\text{V}_2(\text{PO}_4)_3$ nanoparticles and the rmGO sheets, and small particle size. This perfect combination suppresses the growth of $\text{Li}_3\text{V}_2(\text{PO}_4)_3$ nanoparticles, enabling fast electron transport through the underlying graphene layers to $\text{Li}_3\text{V}_2(\text{PO}_4)_3$ nanoparticles and enhancing fast lithium ion diffusion in the particles [25]. It is noted that the relative low capacity retention on cycling between 3.0 and 4.8 V is due to the instability of the electrolyte at high voltages [35].

Cyclic voltammogram (CV) curves of the $\text{Li}_3\text{V}_2(\text{PO}_4)_3/\text{rGO}$ and $\text{Li}_3\text{V}_2(\text{PO}_4)_3/\text{rmGO}$ nanocomposites in the potential ranges of 3.0–4.3 V and 3.0–4.8 V at a scanning rate of 0.05 mV s⁻¹ are shown in Fig. 8a and b. Three pairs of anodic and cathodic peaks (Fig. 8a, labeled as a'/a, b'/b and c'/c) are observed between 3.0 and 4.3 V. The results are in good agreement with the charge–discharge plateaus presented in Fig. 6a and c. The $\text{Li}_3\text{V}_2(\text{PO}_4)_3/\text{rmGO}$ nanocomposite shows more symmetrical and sharper shapes of peaks: the anodic peaks at 3.627, 3.704 and 4.117 V and corresponding cathodic peaks at 3.541, 3.634 and 4.020 V. The separation potentials $\Delta E_{\text{a}-\text{a}'}$, $\Delta E_{\text{b}-\text{b}'}$ and $\Delta E_{\text{c}-\text{c}'}$ of $\text{Li}_3\text{V}_2(\text{PO}_4)_3/\text{rmGO}$ are, respectively, 0.086, 0.070 and 0.097 V, whereas those of $\text{Li}_3\text{V}_2(\text{PO}_4)_3/\text{rGO}$ are, respectively, 0.092, 0.081 and 0.106 V. Similarly, the well-defined peaks and small values of potential interval are also observed between 3.0 and 4.8 V in Fig. 8b, indicating the enhanced electrode reaction reversibility and lower polarization of $\text{Li}_3\text{V}_2(\text{PO}_4)_3/\text{rmGO}$ compared to those of $\text{Li}_3\text{V}_2(\text{PO}_4)_3/\text{rGO}$.

Electrochemical impedance spectroscopy (EIS) was carried out in the full charge state after 4 cycles. Fig. 9 shows the Nyquist plots of $\text{Li}_3\text{V}_2(\text{PO}_4)_3/\text{rGO}$ and $\text{Li}_3\text{V}_2(\text{PO}_4)_3/\text{rmGO}$ in the frequency range between 100 kHz and 10 mHz. Both EIS profiles exhibit a semicircle in the high frequency region and a straight line in the low-frequency region. The intercept impedance on the real axis corresponds to the electrolyte resistance (R_e). The numerical value of the diameter of the semicircle on the Z real axis is approximately equal to the charge transfer resistance (R_{ct}). The low frequency region of the straight line is attributed to the Warburg diffusion of lithium ions into the bulk electrode material. From Fig. 9, the R_{ct} of the $\text{Li}_3\text{V}_2(\text{PO}_4)_3/\text{rmGO}$ (54.8 Ω) is smaller than that of $\text{Li}_3\text{V}_2(\text{PO}_4)_3/\text{rGO}$ (61.7 Ω), indicating that the electrons and Li ions transfer more easily in $\text{Li}_3\text{V}_2(\text{PO}_4)_3/\text{rmGO}$ due to the tight contact between the rmGO sheets and the $\text{Li}_3\text{V}_2(\text{PO}_4)_3$ nanoparticles and the small particle size of $\text{Li}_3\text{V}_2(\text{PO}_4)_3$, which can shorten Li-ion diffusion paths and increase Li ions transport. Thus, the $\text{Li}_3\text{V}_2(\text{PO}_4)_3/\text{rmGO}$

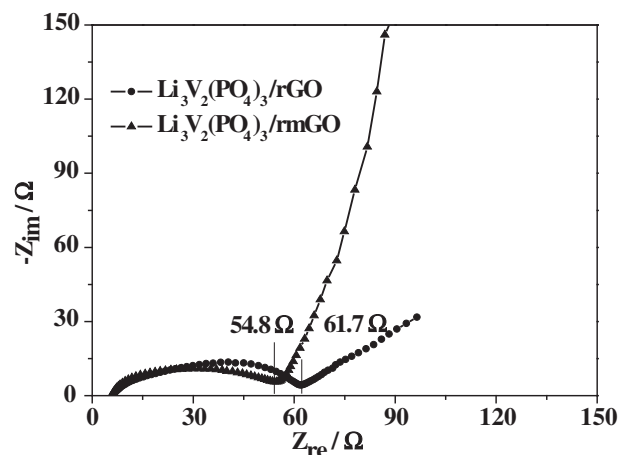


Fig. 9. EIS of $\text{Li}_3\text{V}_2(\text{PO}_4)_3/\text{rGO}$ and $\text{Li}_3\text{V}_2(\text{PO}_4)_3/\text{rmGO}$ in the frequency range between 100 kHz and 10 mHz.

nanocomposite prepared by the present two-step reaction exhibits enhanced electrode reaction kinetics and improved electrochemical performance.

4. Conclusions

We have adopted a two-step reaction for the synthesis of $\text{Li}_3\text{V}_2(\text{PO}_4)_3$ nanoparticles supported on rmGO sheets. First, the mGO with good dispersibility has been synthesized by the insertion of CTAB into lamellar GO sheets. Then, $\text{Li}_3\text{V}_2(\text{PO}_4)_3/\text{rmGO}$ nanocomposites with excellent electrochemical properties have been successfully prepared utilizing mGO through a simple solvothermal method, followed by heat treatment. The $\text{Li}_3\text{V}_2(\text{PO}_4)_3$ nanoparticles deposit on the rmGO sheets, which is attributed to the functional groups of mGO providing sites for the adsorption of cations (V^{3+} and Li^+) and nanoparticles nucleation. The small $\text{Li}_3\text{V}_2(\text{PO}_4)_3$ nanoparticles (~200 nm in size) were attached tightly onto the rmGO sheets due to the large contact between the mGO sheets and the $\text{Li}_3\text{V}_2(\text{PO}_4)_3$ precursor. Compared to the $\text{Li}_3\text{V}_2(\text{PO}_4)_3/\text{rGO}$ nanocomposite, the $\text{Li}_3\text{V}_2(\text{PO}_4)_3/\text{rmGO}$ nanocomposite exhibits better electrochemical properties in terms of capacity, cycle performance, and rate capability. Overall, the study demonstrates that superior electrochemical performance with the insulating $\text{Li}_3\text{V}_2(\text{PO}_4)_3$ could be realized with optimal synthesis and processing approaches.

Acknowledgments

The work at the University of Texas at Austin was supported by the Office of Vehicle Technologies of the U.S. Department of Energy under Contract No. DEAC02-05CH11231 and the work at the Hefei University of Technology was supported by the National Natural Science Foundation of China (NSFC Grants 20976033, 21176054 and 21271058), the Fundamental Research Funds for the Central Universities (2010HGZY0012), and the Education Department of Anhui Provincial Government (TD200702). Bo Pei is grateful to the China Scholarship Council (CSC) Postgraduate Scholarship Program for supporting his stay at the University of Texas at Austin.

References

- [1] M.S. Whittingham, Chem. Rev. 104 (2004) 4271–4301.
- [2] P.S. Herle, B. Ellis, N. Coombs, L.F. Nazar, Nat. Mater. 3 (2004) 147–152.
- [3] B. Pei, Q. Wang, W.X. Zhang, Z.H. Yang, M. Chen, Electrochim. Acta 56 (2011) 5667–5672.

- [4] S.M. Oh, S.W. Oh, C.S. Yoon, B. Scrosati, K. Amine, Y.K. Sun, *Adv. Funct. Mater.* 20 (2010) 3260–3265.
- [5] H. Huang, S.C. Yin, T. Kerr, N. Taylor, L.F. Nazar, *Adv. Mater.* 14 (2002) 1525–1528.
- [6] S.K. Martha, J. Grinblat, O. Haik, E. Zinigrad, T. Drezen, J.H. Miners, I. Exnar, A. Kay, B. Markovsky, D. Aurbach, *Angew. Chem., Int. Ed.* 48 (2009) 8559–8563.
- [7] M.S. Whittingham, Y.N. Song, S. Lutta, P.Y. Zavalij, N.A. Chernova, *J. Mater. Chem.* 15 (2005) 3362–3379.
- [8] S.C. Yin, H. Grondyey, P. Strobel, M. Anne, L.F. Nazar, *J. Am. Chem. Soc.* 125 (2003) 10402–10411.
- [9] M.Y. Saidi, J. Barker, H. Huang, J.L. Swoyer, G. Adamson, *J. Power Sources* 119–121 (2003) 266–272.
- [10] S.Y. Chung, J.T. Bloking, Y.M. Chiang, *Nat. Mater.* 1 (2002) 123–128.
- [11] S.C. Yin, P.S. Strobel, H. Grondyey, L.F. Nazar, *Chem. Mater.* 16 (2004) 1456–1465.
- [12] A.Q. Pan, J. Liu, J.G. Zhang, W. Xu, G.Z. Cao, Z.M. Nie, B.W. Arey, S.Q. Liang, *Electrochem. Commun.* 12 (2010) 1674–1677.
- [13] A.R. Cho, J.N. Son, V. Aravindan, H. Kim, K.S. Kang, W.S. Yoon, W.S. Kime, Y.S. Lee, *J. Mater. Chem.* 22 (2012) 6556–6560.
- [14] C. Deng, S. Zhang, S.Y. Yang, Y. Gao, B. Wu, L. Ma, B.L. Fu, Q. Wu, F.L. Liu, *J. Phys. Chem. C* 115 (2011) 15048–15056.
- [15] C. Wang, H.M. Liu, W.S. Yang, *J. Mater. Chem.* 22 (2012) 5281–5285.
- [16] X.Y. Du, W. He, X.D. Zhang, Y.Z. Yue, H. Liu, X.G. Zhang, D.D. Min, X.X. Ge, Y. Du, *J. Mater. Chem.* 22 (2012) 5960–5969.
- [17] K.S. Novoselov, A.K. Geim, S.V. Morozov, D. Jiang, M.I. Katsnelson, I.V. Grigorieva, S.V. Dubonos, A.A. Firsov, *Nature* 438 (2005) 197–200.
- [18] K.S. Novoselov, Z. Jiang, Y. Zhang, S.V. Morozov, H.L. Stormer, U. Zeitler, J.C. Maan, G.S. Boebinger, P. Kim, A.K. Geim, *Science* 315 (2007) 1379.
- [19] D.A. Dikin, S. Stankovich, E.J. Zimney, R.D. Piner, G.H.B. Domke, G. Evmenenko, S.T. Nguyen, R.S. Ruoff, *Nature* 448 (2007) 457–460.
- [20] C. Lee, X.D. Wei, J.W. Kysar, J. Hone, *Science* 321 (2008) 385–388.
- [21] J.W. Suk, R.D. Piner, J. An, R.S. Ruoff, *ACS Nano* 4 (2010) 6557–6564.
- [22] J. Su, M.H. Cao, L. Ren, C.W. Hu, *J. Phys. Chem. C* 115 (2011) 14469–14477.
- [23] W.W. Zhou, J.P. Liu, T. Chen, K.S. Tan, X.T. Jia, Z.Q. Luo, C.X. Cong, H.P. Yang, C.M. Li, T. Yu, *Phys. Chem. Chem. Phys.* 13 (2011) 14462–14465.
- [24] H.L. Wang, Y. Yang, Y.Y. Liang, L.F. Cui, H.S. Casalongue, Y.G. Li, G.S. Hong, Y. Cui, H.J. Dai, *Angew. Chem., Int. Ed.* 50 (2011) 7364–7368.
- [25] H.D. Liu, P. Gao, J.H. Fang, G. Yang, *Chem. Commun.* 47 (2011) 9110–9112.
- [26] W.S. Hummers, R.E. Offeman, *J. Am. Chem. Soc.* 80 (1958) 1339.
- [27] Y.Y. Liang, D.Q. Wu, X.L. Feng, K. Müllen, *Adv. Mater.* 21 (2009) 1679–1683.
- [28] R.F. Nie, J.H. Wang, L.N. Wang, Y. Qin, P. Chen, Z.Y. Hou, *Carbon* 50 (2012) 586–596.
- [29] H.K. Jeong, Y.P. Lee, Rob J.W.E. Lahaye, M.H. Park, K.H. An, I.J. Kim, C.W. Yang, C.Y. Park, R.S. Ruoff, Y.H. Lee, *J. Am. Chem. Soc.* 130 (2008) 1362–1366.
- [30] T.F. Yeh, J.M. Syu, C. Cheng, T.H. Chang, H. Teng, *Adv. Funct. Mater.* 20 (2010) 2255–2262.
- [31] X.H. Dai, Z.G. Wang, B. Xiao, Y.J. Zhong, C. Wang, C.L. Bai, X.L. Zhang, J. Xu, *Chin. J. Polym. Sci.* 2 (2004) 117–122.
- [32] C.S. Dai, Z.Y. Chen, H.Z. Jin, X.G. Hu, *J. Power Sources* 195 (2010) 5775–5779.
- [33] C. Nethravathi, M. Rajamathi, *Carbon* 46 (2008) 1994–1998.
- [34] X.H. Rui, N. Ding, J. Liu, C. Li, C.H. Chen, *Electrochim. Acta* 55 (2010) 2384–2390.
- [35] A.V. Murugan, T. Muraliganth, P.J. Ferreira, A. Manthiram, *Inorg. Chem.* 48 (2009) 946–952.